Dalton Transactions

ROYAL SOCIETY OF CHEMISTRY

COMMUNICATION

View Article Online
View Journal | View Issue

Check for updates

Cite this: *Dalton Trans.*, 2025, **54**, 12130

Received 15th May 2025,
Accepted 11th July 2025

DOI: 10.1039/d5dt01140j

rsc.li/dalton

Structural control of μ-hydroxo-μ-peroxodicobalt(III) complex with the 6-hpa dinucleating ligand to enhance O_2-evolution activity in catalytic water oxidation†

Yuki Tanaka,[a] Osamu Iwanaga,[a] Kyosuke Fujikawa,[a] Seina Shinomiya,[a] Hiroaki Kitagishi,[a] Sachiko Yanagisawa,[b] Minoru Kubo,[b] Tetsuya Kambe,[c] Shigenobu Masaoka[c] and Masahito Kodera *[a]

The 6-hpa ligand forms a μ-hydroxo-μ-peroxodicobalt(III) complex $[Co(\mu\text{-}OH)(\mu\text{-}O_2)(6\text{-hpa})]X_3$ (X = ClO_4 (1a) and PF_6 (1b)) and controls the formation of *syn* configuration. Electrochemical studies revealed that the 6-hpa ligand lowers the oxidation potential of the peroxide moiety by 0.13 V and twice enhances O_2 evolution during catalytic water oxidation by fixing the *syn* configuration.

The development of sustainable systems is attracting great social attention, given the mounting global warming and energy problems.[1] Oxygen evolution by the O_2-evolving complex (OEC), a Mn_4CaO_5 cluster, during photosynthesis in plant cells is a key reaction essential for sustainable systems.[2] In 1982, Meyer reported a diruthenium complex, so-called the blue dimer, as the first artificial water oxidation catalyst.[3] Recently, various cheap and abundant metals[4] such as Mn,[5] Fe,[6] and Co[7] have been used instead of expensive and rare Ru for water oxidation catalysts.

Thapper reported that the μ-hydroxo-μ-peroxodicobalt(III) complex with the tpa ligand (tris(2-pyridylmethyl)amine) $[Co(\mu\text{-}OH)(\mu\text{-}O_2)(tpa)_2](ClO_4)_3$ (**2**) catalyses O_2 evolution *via* water oxidation in a photochemical reaction.[8] Lue claimed that **2** decomposes to give CoO_x nanoparticles, deposited on the electrode in the electrolytic reaction, to catalyze the reaction as heterogeneous catalysts.[9] Kojima reported that **2-*syn*** and **2-*anti***, diastereomers of **2**, show different O_2-evolving activity.[10]

We have reported diiron[11] and dicopper[12] complexes with the 6-hpa ligand (1,2-bis{2-[bis(2-pyridylmethyl)aminomethyl]-6-pyridyl}-ethane), where a $-CH_2CH_2-$ tether connects two tpa units. The chemical structures of tpa and 6-hpa are shown in Fig. 1. The 6-hpa ligand enabled the conversion between peroxodiiron(III) and dioxodiiron(IV) species *via* reversible O–O bond scission and formation, where the 6-hpa ligand stabilizes these two species.[13] In this study, we report the synthesis, structure, and catalytic water oxidation of μ-hydroxo-μ-peroxodicobalt(III) complexes with 6-hpa $[Co(\mu\text{-}OH)(\mu\text{-}O_2)(6\text{-hpa})]X_3$ (X = ClO_4 (**1a**) and PF_6 (**1b**)) and the effect of 6-hpa ligand fixing the *syn* configuration on the O–O bond formation in catalytic water oxidation.

The ClO_4 salt **1a** was obtained as dark-blue crystals upon reaction of 6-hpa ligand with $Co(ClO_4)_2{\cdot}6H_2O$ in the presence of Et_3N in MeOH under O_2; the crystals were used for the spectroscopic and electrochemical studies. The PF_6 salt **1b** was prepared for the structure analysis. The synthetic details of **1a** and **1b** are shown in the ESI.†

The peroxodicobalt(III) complexes **1b**, **2-*syn***, and **2-*anti*** were structurally characterized by X-ray analysis (Fig. S1:† ORTEP views of **2-*syn*** and **2-*anti***; Table S1:† the crystallographic data; and Tables S2, S3, and S4:† selected bond distances and

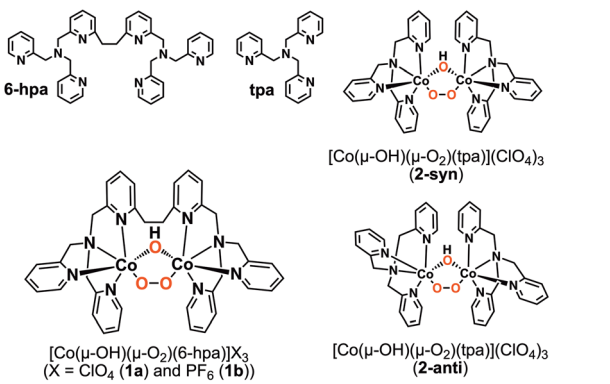

Fig. 1 Chemical structures of ligands and Co complexes.

[a]*Department of Molecular Chemistry and Biochemistry, Doshisha University, Kyotanabe, Kyoto 610-0321, Japan. E-mail: mkodera@mail.doshisha.ac.jp*
[b]*Graduate School of Science, University of Hyogo, 3-2-1 Kouto, Kamigori, Ako, Hyogo 678-1297, Japan*
[c]*Division of Applied Chemistry, Graduate School of Engineering, Osaka University, 2-1 Yamadaoka, Suita, Osaka 565-0871, Japan*

†Electronic supplementary information (ESI) available: Detailed experimental procedures, Fig. S1–S5, Tables S1–S6. CCDC 2415276. For ESI and crystallographic data in CIF or other electronic format see DOI: https://doi.org/10.1039/d5dt01140j

angles of **1b**, **2-*syn***, and **2-*anti***; ESI†). The ORTEP view of **1b** is shown in Fig. 2. The 6-hpa ligand encapsulates a μ-OH-μ-O_2-Co(III)$_2$ core to take the *syn* configuration, where the –CH_2CH_2– tether makes *anti* configuration impossible. This is the structural control by the 6-hpa ligand. Compound **1b** is structurally similar to the *syn* configuration of **2-*syn*** but not to the *anti* configuration of **2-*anti***. The Co···Co and O–O bond distances of 3.254 and 1.395 Å in **1b** are close to the 3.255 and 1.383 Å in **2-*syn*** and longer than the 3.246 and 1.356 Å in **2-*anti***.[15] The Co–O–O–Co dihedral angle 53.4(3)° in **1b** is far smaller than the 61.2(4)° and 63.4(4)° in **2-*syn*** and **2-*anti***.[15] Thus, the dicobalt core of **1b** is more planar than those of **2-*syn*** and **2-*anti***.[16] The average Co–$O_{peroxide}$ bond distance of 1.842 Å in **1b** is slightly shorter than the 1.851 Å and 1.865 Å in **2-*syn*** and **2-*anti***.[15] The short Co–$O_{peroxide}$ bond and planar core structure makes the dπ–pπ interactions of Co–$O_{peroxide}$ bonds stronger in **1b**.

The structure of the 6-hpa complex **1a** in solution was spectroscopically examined. The ^{1}H NMR spectra of **1a** and of a mixture of **2-*syn*** and **2-*anti***, measured in a deuterated Britton–Robinson (B–R) buffer,[14] are shown in Fig. S2 and S3 (ESI)† along with the peak assignments in Tables S5 and S6 (ESI),† respectively. The ^{1}H NMR signals of **2-*syn*** and **2-*anti*** were assigned according to the literature.[10] In the chemical shifts of 6-H atoms in equatorial py groups, the 9.48 ppm red color *a* in **2-*syn*** is higher than the 9.40 and 9.27 ppm purple color *a* and *a*′ in **2-*anti*** (Fig. S3 and Table S6, ESI†), and the 9.48 and 9.40 ppm of 6-H atoms close to μ-O_2 are higher than the 9.27 ppm of that close to μ-OH. The integral ratio (*a* in **2-*syn***) : (*a* in **2-*anti***) : (*a*′ in **2-*anti***) = 2 : 1.4 : 1.4. Since **2-*syn*** has two equivalent 6-H atoms, the ratio of **2-*syn*** : **2-*anti*** is 1 : 1.4. The assymmetric unit in the ^{1}H NMR spectrum of **1a** (Fig. S2, ESI†) is half of a molecular structure because **1a** takes only *syn* configuration. Two equivalent equatorial py groups in **1a** give four signals: a, c, d, and f. The two types among the four axial py groups of **1a** are the pendant py groups and py groups connected by a –CH_2CH_2– tether, giving four signals (b, e, g, h) for the former and two signals (i, j) for the latter (Fig. S2 and Table S5, ESI†). The integration ratios are (a, c, d, f) : (b, e, g, h) = 1 : 1 and i : j = 2 : 1. The chemical shift of 9.87 ppm for the 6-H of the equatorial py group in **1a** is much higher than the 9.48 ppm in **2-*syn*** because the *syn* configuration of **1a** is tightly fixed by the 6-hpa ligand.

Resonance Raman spectra of **1a** and the mixture of **2-*syn*** and **2-*anti*** in MeCN at −30 °C are shown in Fig. 3(A) and (B), respectively. Compound **1a** gave a single O–O stretching vibration band, and the mixture of **2-*syn*** and **2-*anti*** gave two bands. These are consistent with the crystal structures and ^{1}H NMR spectra showing that the 6-hpa ligand forms only the *syn* form, and for the tpa ligand, both the *syn* and *anti* forms. Since the ratio of **2-*syn*** and **2-*anti*** is 1 : 1.4, as shown by the ^{1}H NMR spectrum, the $\nu_{16O-16O}$ band at 845 cm^{-1} of slightly weaker intensity is assigned to **2-*syn***, and that at 866 cm^{-1} to **2-*anti***. These are close to the $\nu_{16O-16O}$ bands 844 and 874 cm^{-1} reported for **2-*syn*** and **2-*anti***.[10] The $\nu_{18O-18O}$ bands of **2-*syn*** and **2-*anti*** prepared under $^{18}O_2$ appeared at 794 and 816 cm^{-1}, and the isotope shifts are 51 and 50 cm^{-1}, respectively. Compound **1a** showed the $\nu_{16O-16O}$ band at 867 cm^{-1} and the $\nu_{18O-18O}$ band at 820 cm^{-1}. The isotope shift is 47 cm^{-1}. This value is close to 49.6 cm^{-1}, the theoretically calculated isotope shift for **1a** shown in ESI.† The $\nu_{16O-16O}$ band 867 cm^{-1} of **1a** is higher by 22 cm^{-1} than the 845 cm^{-1} of **2-*syn***, indicating that the O–O bond of **1a** is strengthened by the 6-hpa ligand encapsulating the μ-OH-μ-O_2-Co(III)$_2$ core.

The electrochemical properties of **1a** and the mixture of **2-*syn*** and **2-*anti*** were compared in the cyclic voltammograms (CV) and square wave voltammograms (SWV) measured in B–R buffer under N_2. In the CV at pH 8.0 (Fig. S4, ESI†), **1a** shows a large oxidation wave at the onset potential of 1.2 V *vs.* NHE, with small reduction and oxidation waves at 0.6 and 1.0 V *vs.* NHE, but **2-*syn*** and **2-*anti*** showed a relatively small oxidation wave at the onset potential of 1.2 V *vs.* NHE, with unclear redox waves in the low-potential region. In the SWV at pH 8.0 (Fig. 4), **1a** and the mixture of **2-*syn*** and **2-*anti*** show two redox

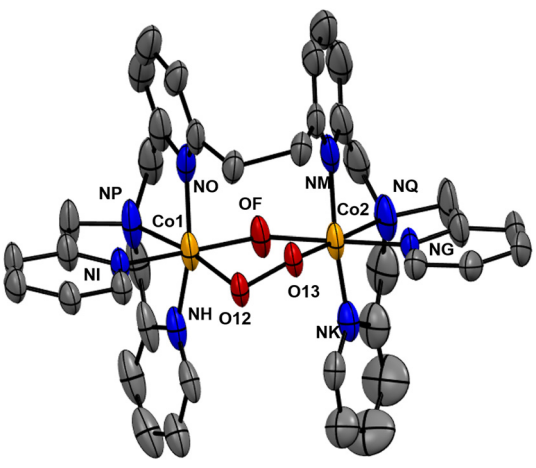

Fig. 2 ORTEP diagram of **1b**. H-atoms are omitted for clarity.

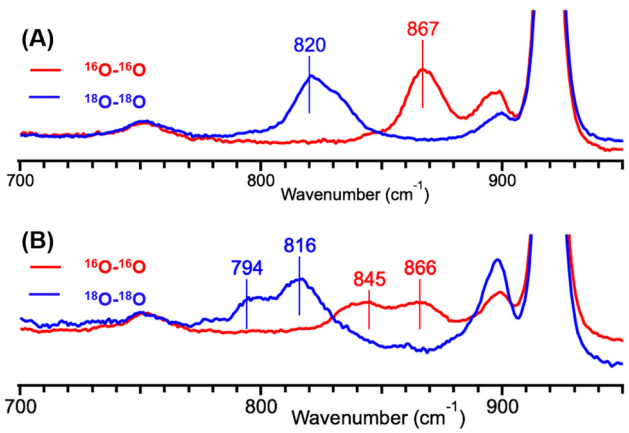

Fig. 3 Resonance Raman spectra of **1a** (A) and a mixture of **2-*syn*** and **2-*anti*** (B) in MeCN at −30 °C with excitation at 405 nm. The spectra of ^{16}O–^{16}O and ^{18}O–^{18}O complexes are shown as red and blue lines, respectively.

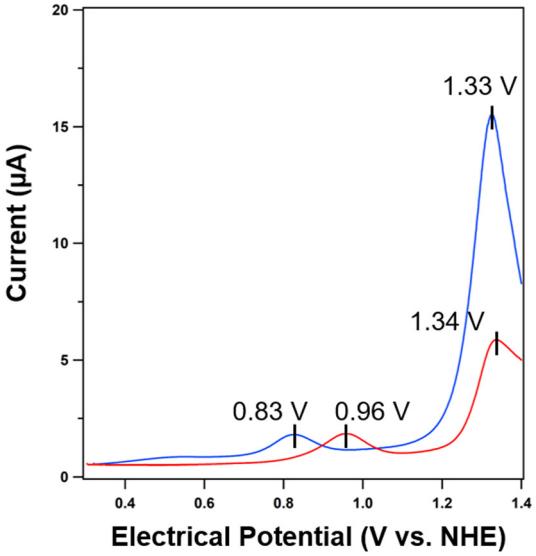

Fig. 4 SWV traces of **1a** (blue) and the mixture of **2-*syn*** and **2-*anti*** (red) (0.1 mM) in B–R buffer at pH 8.0 at 298 K, using a 3 mm GC working electrode (0.07 cm^2), Pt wire counter electrode, Ag/AgCl reference electrode, potential increase: 0.001 V, amplitude: 0.025 A, frequency: 10 Hz, and sensitivity: 10 mA V^{-1}.

peaks at 0.83 and 1.32 V for **1a** and at 0.96 and 1.34 V for the mixture. The low-potential peak is assigned to the oxidation of peroxide moiety, and the high-potential peak to catalytic water oxidation. The low-potential peak at 0.83 of **1a** is lower by 0.13 V than the 0.96 V of **2-*syn*** and **2-*anti***. This is because the dπ–pπ interaction in the Co–$O_{peroxide}$ bond of **1a** is stronger than those of **2-*syn*** and **2-*anti***. The strong dπ–pπ interaction increases the energy level of the anti-bonding orbital of the peroxide O atom to lower the oxidation potential. The catalytic current of water oxidation by **1a** is 2.7-fold higher than that by the tpa complexes. This shows that the 6-hpa ligand enhances the catalytic activity in the water oxidation of **1a** by fixing the *syn* form.

Fig. 5 shows the Pourbaix diagram of **1a** and the mixture of **2-*syn*** and **2-*anti*** based on the SWV data (Fig. S5, ESI†) measured in a pH 3.0–8.0 range. The first redox peak of **1a** is 0.95 V *vs.* NHE in the pH 3.0–5.5 region and shifts negatively from 0.94 to 0.83 V with a slope of 44 mV per pH in the pH 5.5–8.0 region. The second peak of **1a** shifts negatively with a slope of 40 mV per pH from 1.45 to 1.39 V in the pH 4.0–5.5 region and is the same potential of zero slope in the pH 5.5–6.5 region. These slopes are almost the same as the 45 mV per pH reported for **2-*syn*** and **2-*anti***.[10] The first and second peaks are assigned to oxidations of the peroxide moiety to form superoxo species and Co(III) to Co(IV), as reported for **2-*syn*** and **2-*anti***.[10] The redox potential of the peroxide moiety of **1a** is lower by 0.13–0.15 V than those of **2-*syn*** and **2-*anti***, but that of Co(III) to Co(IV) is slightly higher in **1a** than in **2-*syn*** and **2-*anti***. Thus, the dπ–pπ interaction is strengthened by the 6-hpa ligand, which facilitates the oxidation of peroxide moiety and slightly raises the redox potential of Co(III) to Co

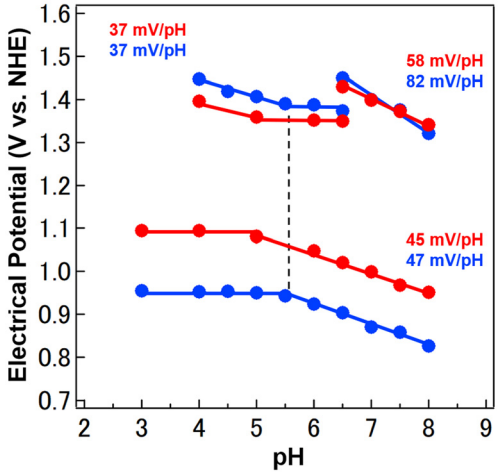

Fig. 5 Plots of redox potentials *vs.* pH values (Pourbaix diagram) for **1a** (blue) and the mixture of **2-*syn*** and **2-*anti*** (red) in B–R buffer at 298 K. The mV per pH values are shown.

(IV). The third peak of **1a** shifted negatively, with a slope of 87 mV per pH from 1.45 to 1.32 V, in the pH 6.5–8.0 region and gave a large catalytic current in the water oxidation. This is much larger than the 27.5 mV per pH reported for the $2e^-$ oxidation and $1H^+$ release process in water oxidation by a $[Co^{III}(\mu\text{-OH})tpa]_2$ complex.[10] The large slope indicates that $2e^-/H^+$ or $4e^-/2H^+$ PCET is involved as a key reaction in the catalytic water oxidation by **1a**.

Controlled potential electrolyses (CPE) of **1a** and the mixture of **2-*syn*** and **2-*anti*** were performed at 1.4 V (*vs.* NHE) in B–R buffer at pH 6.0, 7.0, and 8.0. The O_2 generated during electrolysis was determined by GC analysis. Fig. 6 shows a plot of the turnover number (TON = moles of O_2 generated/moles of complex used) *vs.* reaction time. The time courses of O_2 evolution are composed of two parts, a first rapid reaction and the next slow one. The TON of O_2 evolution at the beginning of 3 h increased with increasing pH, showing that PCET is a key reaction in the catalytic water oxidation. Therefore, the first

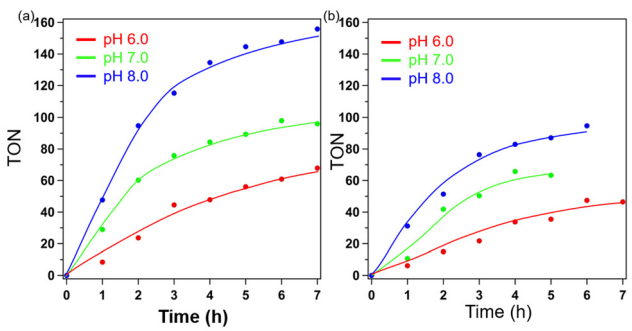

Fig. 6 The controlled potential electrolysis of **1a** (a) and a mixture of **2-*syn*** and **2-*anti*** (b) (0.1 mM) was carried out at 1.4 V (*vs.* NHE) in B–R buffer at pH 6.0, 7.0, and 8.0. Conditions: working electrode Pt mesh, counter electrode Pt wire, reference electrode Ag/AgCl. The amount of O_2 evolution in the CPE was determined by GC analysis.

rapid O_2 evolution is catalysed by the Co complex. However, the O_2 evolution after 3 h did not depend on the pH and kind of Co complex used. This is totally different from the O_2 evolution by Co complexes. The slow O_2 evolution may be catalysed by CoO_x generated in the electrolytic reaction, as reported by Lue *et al.* (Fig. S8 and S9† for CoO_x formation). Thus, the reactions in the beginning of 3 h are used to compare the O_2 evolution activity of the Co complexes. The O_2 evolution by **1a** is two-fold higher than that by a mixture of **2-*syn*** and **2-*anti***. This is consistent with the 2.7-fold larger current of **1a** than those of **2-*syn*** and **2-*anti*** observed in the SWV at 1.3 V. These results show that the *syn* configuration, fixed the by 6-hpa ligand, is a key feature enhancing O_2 evolution in water oxidation by the 6-hpa Co complex. The UV-vis spectral change and current plot in the electrolytic water oxidation of **1a** (Fig. S7†) showed that the LMCT band of **1a** at 384 nm (Fig. S6†) rapidly decreased by the oxidation of peroxide moiety, where a superoxo species A, having absorption at 311 nm, was formed transiently and converted to an intermediate B having absorption at 271 nm kept in the steady-state O_2 evolution.

The mechanism of the O_2 evolution by **1a** is proposed based on the results described above. The electrochemical data showed that the O_2 release of **1a** proceeds *via* successive electron oxidations from the peroxide moiety and Co(III) to Co(IV), similarly to that of **2-*syn*** and **2-*anti*.**[10] Water oxidation after the O_2 release of **1a** may proceed in a $4e^-/2H^+$ PCET of $[Co^{III}–OH]_2$, assignable to intermediate B, where the $2e^-/2H^+$ PCET of $[Co^{III}–OH]_2$ to form $[Co^{III}–O^{\bullet}]_2$, O–O bond formation of $[Co^{III}–O^{\bullet}]_2$, and $2e^-$ oxidation of the resultant peroxo complex successively occur (Scheme 1). As previously reported, the syn-μ-oxodioxodiiron(IV) of 6-hpa ligand forms an O–O bond, and DFT studies revealed that this O–O bond formation is energetically more favourable than the *syn*-to-*anti* transformation of the *syn*-dioxo form.[13] Thus, the *syn* form of $[Co^{III}–O^{\bullet}]_2$, fixed by the 6-hpa ligand, facilitates the O–O bond formation. This is the reason that the 6-hpa complex enhances water oxidation. The O_2 evolution in the CPE at 1.4 V is less likely to be affected by the difference in redox potentials of 1.32 and 1.34 V in water oxidation by **1a** and by the mixture of **2-*syn*** and **2-*anti***, respectively. Thus, the most important feature in the enhancement of catalytic activity by **1a** is structural control by the 6-hpa ligand, fixing the *syn* form of $[Co^{III}–O^{\bullet}]_2$ to facilitate O–O bond formation.

The apparent catalytic rate constant (TOF s^{-1}) of **1a** in the OER at pH 8.0 was estimated to be 430 s^{-1} using the plateau-ing current in the CVs (Fig. S10†), according to the literature.[17] The plot is shown in Fig. S11.† This value is relatively large in water oxidation catalysts,[4b] though smaller than the 1900 s^{-1} of Masaoka's pentairon complex.[6b]

In this study, we synthesized and structurally characterized a new μ-OH-μ-O_2-Co(III)$_2$ complex with 6-hpa ligand $[Co(\mu\text{-}OH)(\mu\text{-}O_2)(6\text{-hpa})]X_3$ (X = ClO_4 (**1a**) and PF_6 (**1b**)) and found that the 6-hpa ligand enhances the catalytic activity of the Co complex in the O_2 evolution by water oxidation, by structurally controlling and fixing the *syn* configuration.

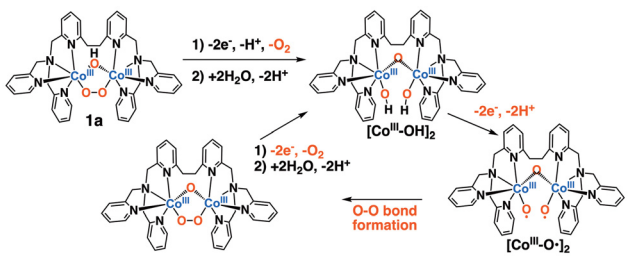

Scheme 1 Proposed mechanism for O_2-evolution by **1a**.

Conflicts of interest

There are no conflicts to declare.

Data availability

The data supporting this article have been included as part of the ESI.†

References

1 D. Welsby, J. Price, S. Pye and P. Ekins, *Nature*, 2021, **597**, 230–234.
2 (*a*) P. Joliot, G. Barbieri and R. Chabaud, *Photochem. Photobiol.*, 1969, **10**, 309–329; (*b*) B. Kok, B. Forbush and M. Mcgloin, *Photochem. Photobiol.*, 1970, **11**, 457–475; (*c*) A. Zouni, H.-T. Witt, J. Kern, P. Fromme, N. Krauss, W. Saenger and P. Orth, *Nature*, 2001, **409**, 739–743; (*d*) Y. Umena, K. Kawakami, J. R. Shen and N. Kamiya, *Nature*, 2011, **473**, 55–60.
3 S. W. Gersten, G. J. Samuels, T. J. Meyer and N. Carolina, *J. Am. Chem. Soc.*, 1982, **104**, 4029–4030.
4 (*a*) M. Kondo and S. Masaoka, *Acc. Chem. Res.*, 2020, **53**, 2140–2151; (*b*) M. Kondo, H. Tatewaki and S. Masaoka, *Chem. Soc. Rev.*, 2021, **50**, 6790–6831.
5 (*a*) M. Calvin, *Science*, 1974, **184**, 375–381; (*b*) K. J. Young, B. J. Brennan, R. Tagore and G. W. Brudvig, *Acc. Chem. Res.*, 2015, **48**, 567–574; (*c*) W. T. Lee, S. B. Muñoz III, D. A. Dickie and J. M. Smith, *Angew. Chem., Int. Ed.*, 2014, **53**, 9856–9859; (*d*) A. K. Poulsen, A. Rompel and C. J. McKenzie, *Angew. Chem., Int. Ed.*, 2005, **44**, 6916–6920.
6 (*a*) L. D. Wickramasinghe, R. Zhou, R. Zong, P. Vo, K. J. Gagnon and R. P. Thumme, *J. Am. Chem. Soc.*, 2015, **137**, 13260–13263; (*b*) M. Okamura, M. Kondo, R. Kuga, Y. Kurashige, T. Yanai, S. Hayami, V. K. K. Praneeth, M. Yoshida, K. Yoneda, S. Kawata and S. Masaoka, *Nature*, 2016, **530**, 465–468; (*c*) K. G. Kottrup and D. G. H. Hetterscheid, *Chem. Commun.*, 2016, **52**, 2643–2646; (*d*) J. L. Fillol, Z. Codolà, I. Garcia-Bosch, L. Gómez, J. J. Pla and M. Costas, *Nat. Chem.*, 2011, **3**, 807–813.
7 (*a*) P. Sharma, S. Gupta, R. Kumar, A. Charisiadis, M. Sauban, L. Velasco, A. Saini, A. Charisiadis, D. Moonshiram and A. Draksharapu, *Chem. Commun.*,

2024, **60**, 14846–14849; (*b*) T. Nakazono, R. Mitsuda, K. Hashimoto, T. Wada and H. Tamiaki, *Inorg. Chem.*, 2024, **63**, 24041–24048; (*c*) T. Nakazono and T. Wada, *Inorg. Chem.*, 2021, **60**, 1284–1288; (*d*) D. J. Wasylenko, R. D. Palmer, E. Schott and C. P. Berlinguette, *Chem. Commun.*, 2012, **48**, 2107–2109; (*e*) H. Y. Du, S. C. Chen, X. J. Su, L. Jiao and M. T. Zhang, *J. Am. Chem. Soc.*, 2018, **140**, 1557–1565; (*f*) D. K. Dogutan, R. McGuire and D. G. Nocera, *J. Am. Chem. Soc.*, 2011, **133**, 9178–9180; (*g*) D. Wang and J. T. Groves, *Proc. Natl. Acad. Sci. U. S. A.*, 2013, **110**, 15579–15584.

8 H.-Y. Wang, E. Mijangos, S. Ott and A. Thapper, *Angew. Chem., Int. Ed.*, 2014, **53**, 14499–14502.

9 J.-W. Wang, P. Sahoo and T.-B. Lu, *ACS Catal.*, 2016, **6**, 5062–5068.

10 (*a*) T. Ishizuka, A. Watanabe, H. Kotani, D. Hong, K. Satonaka, T. Wada, Y. Shiota, K. Yoshizawa, K. Ohara, K. Yamaguchi, S. Kato, S. Fukuzumi and T. Kojima, *Inorg. Chem.*, 2016, **55**, 1154–1164; (*b*) H. Kotani, D. Hong, K. Satonaka, T. Ishizuka and T. Kojima, *Inorg. Chem.*, 2019, **58**, 3676–3682.

11 M. Kodera, M. Itoh, K. Kano, T. Funabiki and M. A. Reglier, *Angew. Chem., Int. Ed.*, 2005, **44**, 7104–7106.

12 (*a*) T. Tsuji, A. A. Zaoputra, Y. Hitomi, K. Mieda, T. Ogura, Y. Shiota, K. Yoshizawa, H. Sato and M. Kodera, *Angew. Chem., Int. Ed.*, 2017, **56**, 7779–7782; (*b*) H. Takahashi, K. Wada, K. Tanaka, K. Fujikawa, Y. Hitomi, T. Endo and M. Kodera, *Bull. Chem. Soc. Jpn.*, 2022, **95**, 1148–1155.

13 (*a*) M. Kodera, Y. Kawahara, Y. Hitomi, T. Nomura, T. Ogura and Y. Kobayashi, *J. Am. Chem. Soc.*, 2012, **134**, 13236–13239; (*b*) M. Kodera, S. Ishiga, T. Tsuji, K. Sakurai, Y. Hitomi, Y. Shiota, P. K. Sajith, K. Yoshizawa, K. Mieda and T. Ogura, *Chem. – Eur. J.*, 2016, **22**, 5924–5936.

14 (*a*) H. T. K. Britton and R. A. Robinson, *J. Chem. Soc.*, 1931, 1456–1462; (*b*) R. Wang, J. G. Vos, R. H. Schmehl and R. Hage, *J. Am. Chem. Soc.*, 1992, **114**, 1964–1970.

15 The difference in O–O bond distance 0.039 Å between **1b** and **2-*anti*** is larger than 3σ = 0.012 and 0.027 Å in **1b** and **2-*anti***, respectively. The differences in Co–O–O–Co dihedral angles 7.8° and 10.0° between **1b** and **2-*syn***, and **1b** and **2-*anti*** are much larger than 3σ = 0.9°, 1.2°, 1.8° in **1b**, **2-*syn***, **2-*anti***, respectively. The difference in average Co–$O_{peroxide}$ bond distance 0.023 Å between **1b** and **2-*anti*** is larger than 3σ = 0.09 Å in **1b** and close to 0.024 Å in **2-*anti***. These differences are meaningful.

16 Mean plane distances of Co, Co, O, O in the Co–O–O–Co of **1b**, 0.111, 0.110, 0.281, 0.282 Å, are significantly smaller than 0.121, 0.125, 0.329, 0.325 Å of **2-*syn*** and 0.122, 0.124, 0.340, 0.338 Å of **2-*anti***.

17 C. Costentin, S. Drouet, M. Robert and J.-M. Savéant, *Science*, 2012, **338**, 90–94.